
A NUMERICAL INVESTIGATION OF TBA.....!!!1

BY H.G.K.G JAYATUNGA

A THESIS SUBMITTED TO MONASH UNIVERSITY IN FULFILMENT OF THE REQUIREMENTS
FOR THE DEGREE OF

DOCTOR OF PHILOSOPHY

Department of Mechanical Engineering

Monash University

Date!!!!!!

CONTENTS

1	A review of the literature	1
1.1	Flow induced vibrations	1
1.2	Fluid-elastic galloping	1
1.2.1	Excitation of galloping	1
1.2.2	Quasi-steady state theory	2
1.2.3	Induced force and the shear layers	5
1.2.4	Frequency response	7
1.2.5	Fluid mechanics governing the galloping response	7
1.2.6	Galloping as a mechanism of energy harvesting	8
2	Methodology and validation	11
2.1	Introduction	11
2.1.1	Parameters used	11
2.2	Quasi-steady model	12
	Solving the quasi-steady state equation	13
2.3	Calculation of average power	13
	Direct numerical simulations (DNS)	14
	Boundary conditions	14
	Spectral element method	15
2.3.1	Convergence and validation studies	15
	Domain size	15
	Convergence	15

3	Governing parameters of fluid-elastic galloping	18
3.1	Introduction	18
3.2	Formulation of the non-dimensionalised parameters Π_1 and Π_2	19
3.3	Quasi-steady state results	21
3.3.1	Classical VIV parameters vs. Π_1 and Π_2	21
3.3.2	High and low Re data	22
3.3.3	Dependence on mass-stiffness, Π_1	24
3.3.4	Dependence on the mass ratio m^*	28
3.3.5	Comparison with DNS data	28

CHAPTER 1

A REVIEW OF THE LITERATURE

1.1 Flow induced vibrations

1.2 Fluid-elastic galloping

Fluid-elastic galloping is one of the most commonly observable flow-induced vibration on a slender body. Since this phenomenon is most common in civil structure, such as buildings and iced-transmission lines, the term “aeroelastic galloping” is commonly used as the body is immersed in air. However, this mechanism can occur on a slender body immersed in any Newtonian fluid, provided that the conditions to sustain the galloping mechanism are satisfied. This work is based on a general Newtonian flow, thus the term “ fluid-elastic galloping” is used throughout this thesis.

1.2.1 Excitation of galloping

Païdoussis et al. (2010) describes galloping as a “velocity dependent and damping controlled” phenomenon. Therefore, in order for a body to gallop, an initial excitation has to be given to that body. While this excitation is mainly caused by the force created from vortex shedding, other fluid instabilities may contribute to this initial excitation. When a bluff body moves along the transverse direction of the fluid flow, it generates a force along the transverse direction. This force, also known as the induced lift is a resultant of the velocity of the fluid and the motion of the body. When this body is attached to an

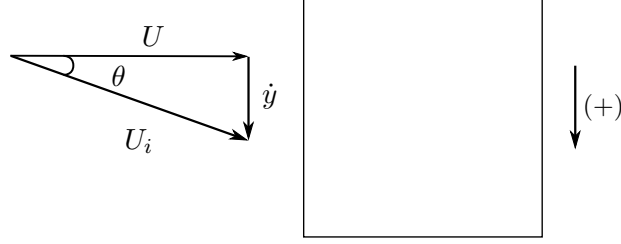


Figure 1.1: Induced angle of attack on the square prism due to the resultant of free-stream velocity of the fluid and transverse velocity of the body.

oscillating system (i.e. a simple spring, mass and damper system), the induced lift becomes the periodic forcing of the system. Galloping is sustained if the induced lift is in phase with the motion of the body. This could be explained further by using a square cross section as an example.

Figure 1.1 illustrates the motion of the body at a given instantaneous time. The induced angle of attack is formed on the square cross section as a result of the free-stream velocity vector U and the transverse velocity vector of the body $y\dot{}$. Thus, a force is formed in phase with the motion of the body (square cross section). This mechanism could also be observed on other bodies which are prone to galloping. The sign convention in this figure (and generally used in this scope of research) states that downward direction is positive. Hence, the force generated on a body under the influence of galloping, could be also identified as a “negative lift”.

1.2.2 Quasi-steady state theory

According Païdoussis et al. (2010), the initial studies by Glauert (1919) provided a criterion for galloping by considering the auto-rotation of a stalled aerofoil. As this phenomenon commonly occur in iced transmission lines, Den Hartog (1956) has provided a theoretical explanation for iced electric transmission lines.

The pioneering study in order to mathematically model galloping was conducted by Parkinson and Smith (1964). This model has been widely used in almost all subsequent studies regarding galloping. A weakly non-linear oscillator model was developed by them to predict the response of the system. Essentially the quasi-steady assumption was made to develop this theory assuming that the instantaneous induced lift force of the oscillating

body is equal to that of the lift force generated by the same body at the same induced angle of attack. In order to satisfy the quasi-steady assumption few conditions had to be satisfied.

- The velocity of the body does not change rapidly
- There is no interaction between vortex shedding and galloping

The second condition is satisfied by ensuring the vortex shedding frequency is much higher than the galloping frequency. The oscillator equation was solved using the Krylov and Bogoliubov method. Details of this method would not be mentioned as it is not used in the present study to solve the oscillator equation. The results obtained from experiments, carried out at $Re = 2200$ and a mass ratio (m^*) around 1164 had a good agreement with the theoretical data which is shown in figure 1.2.

Quasi-steady state oscillator model

The equation of motion of transversely oscillating body is given by

$$m\ddot{y} + c\dot{y} + ky = F_y, \quad (1.1)$$

where the forcing term F_y is given by

$$F_y = \frac{1}{2}\rho U^2 \mathcal{A} C_y. \quad (1.2)$$

As explained previously, when quasi-steady assumption is used the stationary C_y data (which consists of both lift and drag data) of the body could be used as inputs to the oscillator equation. Parkinson and Smith (1964) used a 7th order odd interpolating polynomial to determine C_y . The order of the polynomial can be chosen arbitrarily depending on the study. For example Barrero-Gil et al. (2009, 2010) have used a 3rd order polynomial in order to simplify the analytical model. However, Ng et al. (2005) pointed out that a 7th order polynomial is sufficient as it does not provide a significantly better result.

$$C_y(\theta) = a_1 \left(\frac{\dot{y}}{U} \right) - a_3 \left(\frac{\dot{y}}{U} \right)^3 + a_5 \left(\frac{\dot{y}}{U} \right)^5 - a_7 \left(\frac{\dot{y}}{U} \right)^7. \quad (1.3)$$

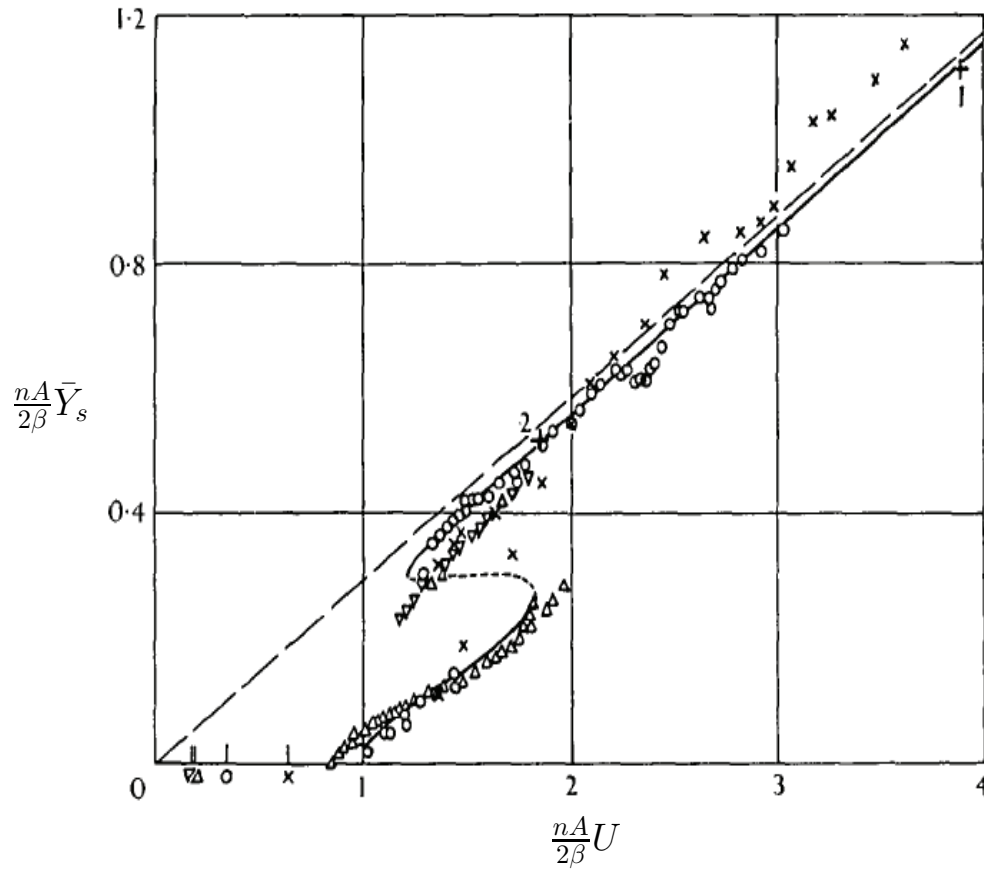


Figure 1.2: “Collapsed amplitude-velocity characteristic. Theory: — stable limit cycle, --- unstable limit cycle. Experiment $\times \beta = .00107$, $\circ \beta = .00196$, $\triangle \beta = .00364$, $\nabla \beta = .00372$, $+1 \beta = .0012$, $+2 \beta = .0032$ Reynolds numbers 4,000 – 20,000 ”. Figure extracted from Parkinson and Smith (1964). $\frac{nA}{2\beta} \bar{Y}_s$ is the dimensionless displacement amplitude parameter and $\frac{nA}{2\beta} U$ is the reduced velocity.

Therefore by substituting the forcing function to the oscillator equation (Eq:1.1) the Quasi-steady state (QSS) model could be obtained (Eq:1.4).

$$m\ddot{y} + c\dot{y} + ky = \frac{1}{2}\rho U^2 \mathcal{A} \left(a_1 \left(\frac{\dot{y}}{U} \right) - a_3 \left(\frac{\dot{y}}{U} \right)^3 + a_5 \left(\frac{\dot{y}}{U} \right)^5 - a_7 \left(\frac{\dot{y}}{U} \right)^7 \right). \quad (1.4)$$

As the current study is focused on the low Re region, it is a known fact that the vortex shedding will be correlated well and therefore provide a significant forcing in the low Reynolds number region. Joly et al. (2012) introduced an additional sinusoidal forcing function to the model in order to integrate the forcing by vortex shedding. By the addition of this forcing Joly et al. (2012) managed to obtain accurate predictions of the displacement amplitude even at low mass ratios, where the galloping is suppressed or not present. Yet, the strength or the amplitude of this sinusoidal forcing has to be tuned in an *ad hoc* manner, and it was not clear the relationship between this forcing with the other system parameters. Thus in the current study this forcing was not used.

Presence of hysteresis

Hysteresis could be observed in the amplitude data of Parkinson and Smith (1964). In contrast, the studies carried out by Barrero-Gil et al. (2009) and Joly et al. (2012) at much lower Reynolds numbers ($159 \leq Re \leq 200$), did not show any hysteresis. Luo et al. (2003) concluded that the hysteresis was present due to the presence of an inflection point in the C_y curve at high Reynolds numbers (Parkinson and Smith (1964) data) which was not present at lower Reynolds numbers. It was further explained and demonstrated by Luo that the inflection point occurs due to the intermittent re attachment of the shear layer in certain angles at high Reynolds numbers.

1.2.3 Induced force and the shear layers

It is important to have an understanding on how the induced lift is generated in a fluid dynamics point of view. The quasi-steady model has already been validated and re-validated by many studies, therefore the flow-field data of static body simulations could be used to analyse the underpinning fluid dynamic mechanisms governing galloping.

The governing mechanism of galloping is the behaviour of the shear layers created at the leading edge due to flow separation on the top and bottom of the body. A common

1. A REVIEW OF THE LITERATURE

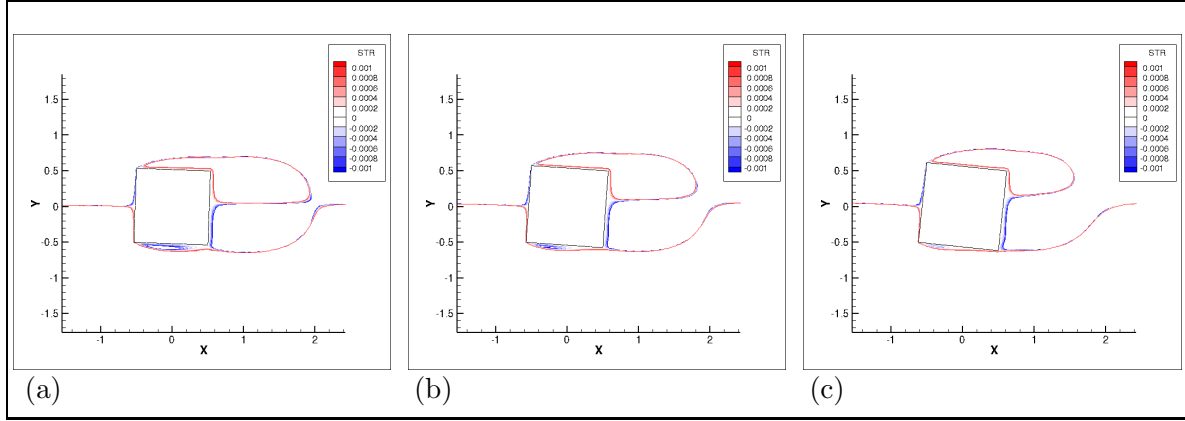


Figure 1.3: Stream functions of time averaged flow field on a stationary square section at $Re = 200$ at different incidence angles. (a) 2° (C_y increases), (b) 4° (C_y peaks) and (c) 2° (C_y decreases). The bottom shear layer comes closer to the bottom wall and reattaches as the angle of incidence increase.

example is a square cross section which has been used widely in studies on galloping. In this square cross section (figure 1.3) the flow separate from the leading edges of the body and create two shear layers on the top and bottom sides of the the body. Figure 1.3 shows the stream functions of time averaged (over a vortex shedding cycle) flow fields of stationary cross sections. The angle of incidence increases clockwise from $2^\circ - 6^\circ$. As θ is increased, the bottom shear comes closer to the wall of the body compared to the top shear layer (Figure 1.3 (a)). The shear layer nearer to the body crates higher suction compared to the shear layer at the opposite side. This pressure imbalance between the top and bottom sides of the body creates a downward force (i.e. the negative lift). As the angle is increased, the bottom shear layer becomes more closer and therefore the pressure difference becomes grater leading to a higher C_y . The negative lift force becomes maximum when the shear layer near to the wall reattaches at the trailing edge (figure 1.3 (b)). As θ is further increased, the bubble in the bottom shear layer shrinks in size resulting the reduction of the pressure imbalance of the top and bottom surface leading to the reduction in C_y . put the cY curve as crodd reference. As the body is connected to an oscillatory system (discussed in section 1.2.1), this shear layer behaviour also harmonize with the cyclic behaviour of the system providing the driving force to the system so that the motion of galloping is sustained.

1.2.4 Frequency response

It is clear that the cyclic motion of the shear layer harmonize with the mechanical system. Therefore, the frequency response should be then, the natural frequency of the system ω_n which much is different from VIV mechanism, where the primary frequency comes from the periodic forcing of the vortex shedding. Hence, in the QSS model the natural frequency of the system could be identified as the frequency of oscillations. However, it should be noted that this is valid on the regimes where the conditions discussed in section 1.2.2 are satisfied.

On the other hand, the forcing function in the QSS model equation 1.4, is a non linear function. As the mass ratio is quite high, the non-linearities of the forcing does not make much effect to the frequency response. However, as the mass ratio goes down theoretically the non linearities of the forcing should affect the frequency response of the system.

The experimental studies carried by Bouclin (1977) concluded at high reduced velocities with large inertia, the motion of the cylinder controls the frequency of the system rather than the vortex shedding. The structural damping has no effect provided that it is small. He also concluded that as the inertia and the reduced velocity gets lower, there is some interaction between vortex shedding and galloping. And at this region the frequency is mainly governed by the vortex shedding.

1.2.5 Fluid mechanics governing the galloping response

As discussed in subsection 1.2.3 the driving force of a galloping system is the asymmetrical placement of the shear layers at either sides of the body. In consequence, it is clear that a significant afterbody is needed for the shear layer interaction to sustain galloping. Parkinson (1974, 1989) and Bearman et al. (1987) have discussed well the importance of the length and the shape for galling in their reviews. It is also highlighted in Parkinson (1974) that the most important physical parameters for galloping are the size relative to the characteristic hight and the shape of the afterbody. Manipulating the shape of the afterbody and thereby, manipulating the shear layer interactions with the body, gives the ability to control the galloping response. Thus, due to this reason work has been carried out on the response of galloping of different cross sectional shapes.

Blevins (1990) provided a good comparison of the shapes which are prone to galloping based on the work by Parkinson and Brooks (1961), Nakamura and Mizota (1975) and Nakamura and Tomonari (1977). The reproduction of Blevins's data could be found in Païdoussis et al. (2010) presented in figure 1.4.

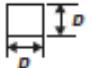
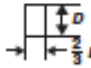
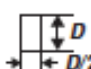

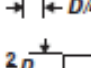
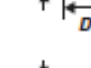
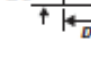
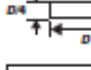
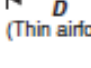



Naudascher and Wang (1993), Ruscheweyh et al. (1996), Deniz (1997) and Weaver and Veljkovic (2005) are some of the work done on different cross sectional shapes. Alonso et al. (2009) carried out wind tunnel tests on biconvex and rhomboidal cross sections. Studies were further carried out by Alonso for elliptical cross sections (Alonso et al., 2010) and triangular cross sections (Alonso et al., 2005). The regions of stability for galloping at different angles of attack and the static force coefficients are presented in these studies with regards to the cross section involved.

1.2.6 Galloping as a mechanism of energy harvesting

The focus on fluid-elastic galloping in the past was on understanding and developing methods to suppress it, due to the adverse effects on civil structures. However, recently, the focus of research has been redirected to develop mechanisms to excite galloping rather than suppressing it. This is due to the recent trend on the search of alternate energy sources with minimal environmental impact have lead researchers working on investigating the possibility of extracting useful energy from flow induced vibrations.

Bernitsas and his group in the University of Michigan have made significant progress on using VIV as potential candidate for energy extraction. Bernitsas et al. (2008) introduced the concept of using VIV as a mode of energy extraction. The group have developed a device called VIVACE converter based on this concept. The work has been further expanded to focus on various aspects (such as Reynolds number effects, damping effects etc.) in Bernitsas et al. (2009); Raghavan et al. (2009); Raghavan and Bernitsas (2011); Lee et al. (2011).

To this end, investigations on the possibility of using fluid-elastic galloping as a mode of energy extraction have not being pursued much. Barrero-Gil et al. (2010) was the first work which placed the concept of using fluid-elastic galloping as a mode of energy harvesting. In his paper Barrero-Gil et al. (2010) clearly explains the advantages of using galloping as a mode of energy harvesting. Unlike VIV, galloping is not a resonant phenomenon which

Section	h/d	$\partial C_{Fy}/\partial \alpha$		Reynolds number
		Smooth flow	Turbulent flow ^b	
	1	3.0	3.5	10^5
	3/2	0.	-0.7	10^5
	2	-0.5	0.2	10^5
	4	-0.15	0.	10^5
	2/3	1.3	1.2	6.6×10^4
	1/2	2.8	-2.0	3.3×10^4
	1/4	-10.	-	$2 \times 10^3 - 2 \times 10^4$
 (Thin airfoil)	- ^c	-6.3	-6.3	$> 10^3$
	-	-6.3	-6.3	$> 10^3$
	-	-0.1	0.	6.6×10^4
	-	-0.5	2.9	5.1×10^4
	-	0.66	-	7.5×10^4

^a α is in radians; flow is left to right. $\partial C_{Fy}/\partial \alpha = -\partial C_{Ll}/\partial \alpha - C_D$, with C_{Fy} based on the dimension D , so that $\partial C_{Fy}/\partial \alpha > 0$ for galloping.

^b Approximately 10% turbulence.

^c Inappropriate to use h/d .

Figure 1.4: “The transverse force coefficient for various sections in steady smooth or turbulent flow (after Blevins (1990))” obtained from Païdoussis et al. (2010)

1. A REVIEW OF THE LITERATURE

needs the synchronisation or “lock-in” and therefore have the following advantages.

- The range where significant oscillations develop is not restricted to a narrow band of frequencies.
- Galloping does not have a self-limited response beyond the critical velocity (Barrero-Gil et al., 2010) and therefore the amplitudes increase as the flow velocity is increased.

CHAPTER 2

METHODOLOGY AND VALIDATION

2.1 Introduction

A brief overview of the computational methods to perform the simulations to obtain the data in this thesis are presented in this chapter. As the this particular study is not focused on developing computational methods but concentrated on understanding the physics of a body under the influence of fluid-elastic galloping, it should be noted that the overview provided in this chapter is quite abstract.

The flow of this chapter is as follows. First the equations used to model the system are presented and

Finally, a series of validation data are presented and discussed to ensure the accuracy of the direct numerical simulations in order to ensure the confidence in the numerical predictions of this thesis.

2.1.1 Parameters used

The data in this project are mainly presented in two categories, high and low Reynolds numbers to compare results at laminar and turbulent range. One main objectives in this study was to capture the flow physics accurately using direct numerical simulations hence, major portion of the study was carried out in the laminar range where the flow is close to 2D. Although majority of data are focused on low Reynolds numbers, some data were presented using inputs from high Reynolds numbers to the QSS model to provide a comparison between high and low Reynolds numbers. $Re = 200$ was defined as the “low” Reynolds

number and $Re = 22300$ was defined as the high Reynolds number. Studies by Tong et al. (2008) and Sheard et al. (2009) reveals that the approximate value of 3-dimensional transition of the wake for a square cross section is $Re = 160$ and therefore, $Re = 200$ was selected to represent the low Reynolds number regime, also considering the fact that other numerical studies in the laminar regime have used this value for the Reynolds number (Robertson et al., 2003; Joly et al., 2012). The reason behind considering the flow regimes of a square cross section was the fact that the basic cross section being used in this study was a square. The selection of the value for the high Reynolds number was fairly simple as it was the Reynolds number where the pioneering study of galloping Parkinson and Smith (1964) provided the experimental input data ($C_y data$) for the QSS model.

Stationary C_y data at different angles of attack to be used as inputs to the QSS model, were obtained for the low Reynolds number regime using direct numerical simulations. The average power was obtained by using equation ??, and the averaging was done over no less than 20 galloping periods. For the high Re tests, predictions of power output at $Re = 22300$ were obtained using the coefficients for the C_y curve from Parkinson and Smith (1964). The mass ratio m^* was kept at 1163 for $Re = 22300$ (Similar to Parkinson and Smith (1964)), $m^* = 20$ for $Re=200$ and $U^* \geq 40$ similar to the parameters used in literature (Robertson et al., 2003; Joly et al., 2012) to obtain a comparison with published work. These parameters were used throughout this study unless otherwise specified.

2.2 Quasi-steady model

The quasi-steady state model discussed in section 1.2.2 was used to obtain oscillator response data. The quasi-steady state model has proven its ability to obtain accurate galloping response data (discussed in section 1.2.2). Therefore, it enables to obtain large number of at the expense of a short computational time. The oscillator equation consist of spring, mass and damper oscillator expression with a 7th order interpolation polynomial as the forcing function (equation 1.4).

Solving the quasi-steady state equation

The quasi-steady model being an ordinary differential equation could be solved using different solving methods. Some of the techniques include limit cycle oscillations, harmonic balance, cell mapping and numerical integration. Vio et al. (2007) showed that numerical integration provides accurate data. A fourth-order Runge-Kutta ODE solving scheme was used in solving the quasi-steady state oscillator equation. The built in ‘ode45’ function in MATLAB was used primarily to solve the QSS equation while in some cases ‘ode15s’ function was used when the equation became more stiff.

2.3 Calculation of average power

The ideal potential amount of harvested power output could be represented as the dissipated power due to mechanical damping before losses in any power take-off system are included. Thus the mean power output could be expressed as

$$P_m = \frac{1}{T} \int_0^T (c\dot{y})\dot{y}dt, \quad (2.1)$$

where T is the period of integration and c is the mechanical damping constant.

The work done on the body by the fluid is equal to this quantity, defined as

$$P_m = \frac{1}{T} \int_0^T F_y \dot{y}dt, \quad (2.2)$$

where F_y is the transverse (lift) force.

The two definitions of the mean power provide two vital interpretations of power transfer. Equation ?? shows that the power is proportional to the mechanical damping and the magnitude of the transverse velocity. At first glance one may assume that the power could be increased by increasing damping. In a practical power extraction device, the significant component of damping would be due to the electrical generator and therefore, an increase in damping would be due to the increase of the load or in other words the electrical resistance. Yet this perception of damping is not quite accurate as very high damping would result in reducing the velocity amplitude which then, would not result in a higher energy output according to equation ?. In consequence, a balance need to be obtained where the

damping is high, but not to the extent that it will adversely result by overly suppressing the motion of the body.

On the other hand, equation ?? shows that a higher power is attained during situations where the transverse force F_y and the transverse velocity are in phase. Hence, a simple increase in the magnitude of the force or the velocity is not satisfactory to attain a higher power transfer. Any increase in magnitude of either of the parameters (force or velocity) is linked to an increase in phase.

Direct numerical simulations (DNS)

Direct numerical simulations were employed to obtain the stationary data to be used as inputs to the QSS model and to obtain fluid-structure interaction (FSI) data to be compared with the QSS model at low Reynolds numbers. A high-order in-house build spectral element which simulates two-dimensional laminar flows was used to obtain the DNS data.

Boundary conditions

The boundary conditions, regardless of the mesh were common for all the simulations performed. A no-slip condition was applied to the cross section wall. This condition implied that the velocity is zero at the surface of the cross section. For stationary simulations a Dirichlet boundary condition and for FSI cases a time-dependent Dirichlet boundary condition was employed for the velocity on the inlet and lateral boundaries. A Dirichlet boundary condition should have a specified value for the variables (Kreyszig, 2010) in this case velocity. The time-dependent Dirichlet condition has to be implemented for the FSI cases to account for the accelerated reference frame attached to the cross section. Thus, the inlet boundary was set to $u = U$ and $v = -\dot{y}$ for FSI cases and $v = 0$ for stationary cases, where u, v are the velocities in the x and y directions, respectively.

A Neumann condition for the pressure (where the gradient of a property is specified Tu et al. (2008)), where the normal gradient was calculated from the Navier–Stokes equations, was employed on the inlet, lateral and body surface (Gresho and Sani, 1987), while a Dirichlet condition for the pressure ($p = 0$ was enforced at the outlet. The details of the method can be found in Thompson et al. (2006, 1996)

Although the physical validity of the outlet boundary condition is not quite true, this

does not turn out to be a significant problem provided that the Reynolds numbers are low and the domain is sufficiently far away from the body.

Spectral element method

To obtain DNS results an in-house build code was used. This code essentially solves the Navier-Stokes equations in an accelerated reference frame. A three-step time-splitting scheme also known as a fractional step method was used for temporal discretisation. A predictor-corrector method was used for the FSI data where an elastically mounted body was involved. A description of the spectral element method in general can be found in Karniadakis and Sherwin (2005). This code has been very well validated in a variety of fluid-structure interaction problems similar to that studied in the current study (Leontini et al., 2007; Griffith et al., 2011; Leontini et al., 2011; Leontini and Thompson, 2013). Therefore, a validation studies for the code, the method and the algorithms are not discussed in this thesis.

2.3.1 Convergence and validation studies

Domain size

For all cases, a rectangular domain was employed where the inlet was placed $20D$ from the centre of the body, while the outlet was situated $60D$ away from the centre of the body. The lateral boundaries were placed $20D$ away from the centre of the body. The macro element arrangement of the general domain is shown figure 2.1 while the element arrangement near the cross sections are presented in figure 2.2.

Convergence

A series of simulations were carried out in order to ensure the results were grid independent. This was done by keeping the layout of the macro element the same and varying the order of the interpolation polynomial (*p-refinement*). The displacement amplitudes were compared against various polynomial orders. The time step was also altered to meet the Courant condition. The summary of the results are presented [The results table](#).

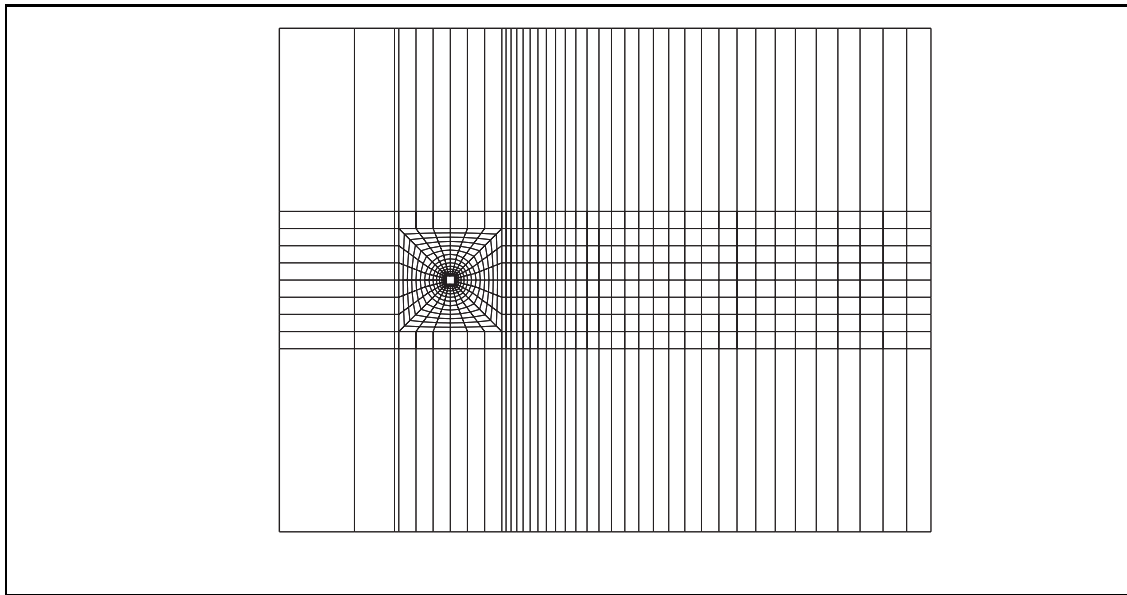


Figure 2.1: Macro element arrangement of the domain of the square cross section. The inlet extending $20D$ towards upstream from the centre of the body, while the outlet extended $60D$ downstream from the centre of the body. The lateral boundaries were placed $20D$ away from the centre of the body

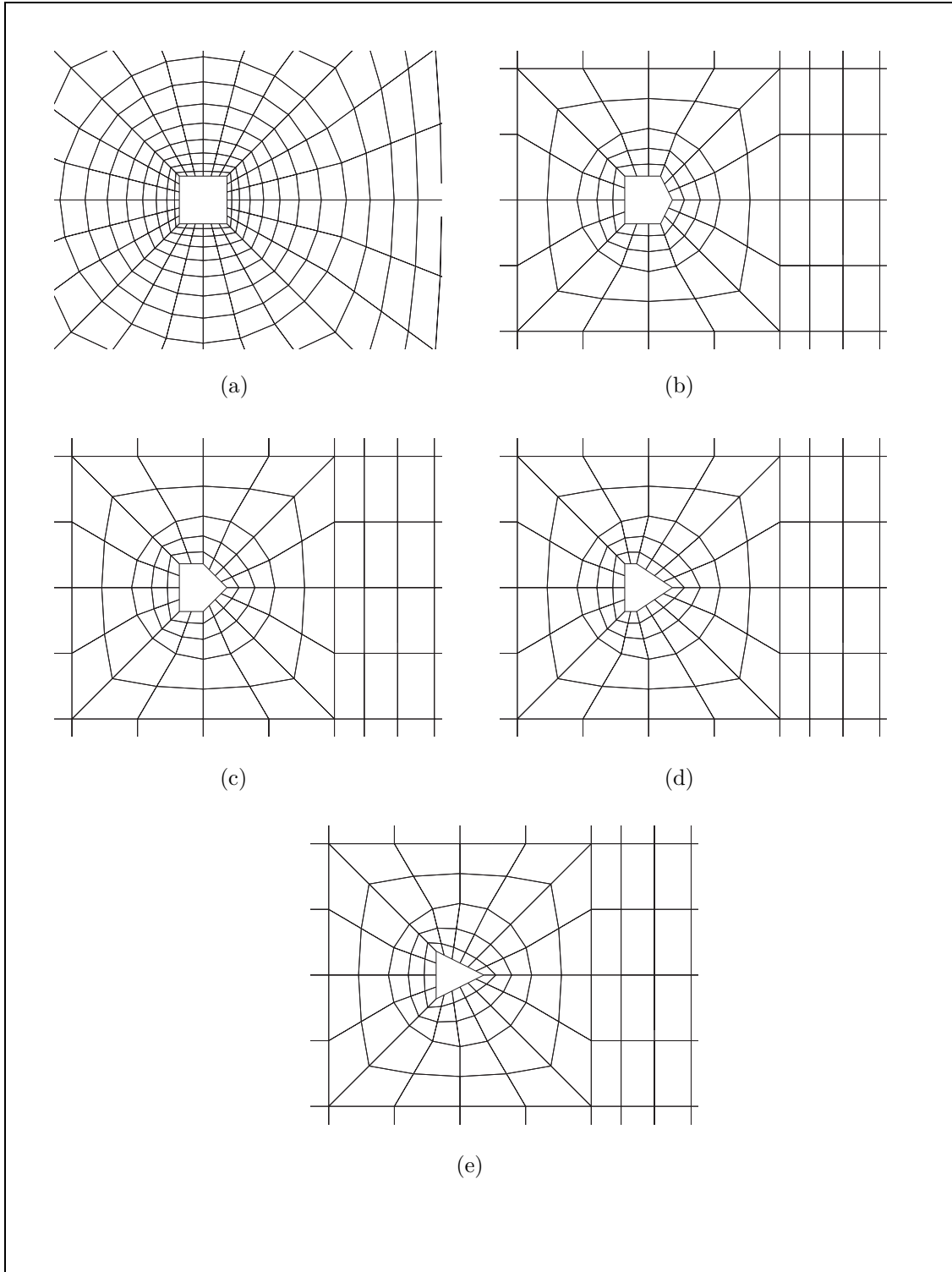


Figure 2.2: Configuration of the macro elements near the cross section. (a) square, (b) $\frac{d}{l} = 0.75$, (c) $\frac{d}{l} = 0.5$, (d) $\frac{d}{l} = 0.25$ and (e) triangle.

CHAPTER 3

GOVERNING PARAMETERS OF FLUID-ELASTIC GALLOPING

3.1 Introduction

This chapter contains the formulation of non dimensional governing parameters namely, the combined mass-stiffness Π_1 and the combined mass-damping Π_2 and the results and discussion demonstrating the influence of them. These parameters are formulated by obtaining the relevant time-scales of the system followed by non-dimesnionlising the governing QSS oscillator equation.

A comparison of Quasi-steady state data presented using the classical VIV parameters and the newly formulated Π_1 and Π_2 is presented and it is concluded that Π_2 provides a better collapse for velocity amplitude and mean power compared the classical reduced velocity (U^*) particularly because unlike U^* , Π_2 does not include a frequency component in it. This is followed by the presentation of QSS data and discussion on the influence of Π_1 and Π_2 on power, which concludes that the power transfer is a primary function of Π_2 and a weak function of Π_1 .

Following this, a comparison of the QSS data with Direct Numerical Simulations (DNS) is presented. This reveals that the power transfer of the DNS data is strongly influenced by both Π_1 and Π_2 . Further analysis reveals that there is a good agreement between QSS and DNS for velocity and power at substantially high Π_1 . As Π_1 decreases, the deviation

(between QSS simulations and DNS) increases. Power spectral analysis of the DNS data shows a significant response at the vortex shedding at low Π_1 . The relative strength was found out to be an inverse function of Π_1 , which provides a clear explanation for the deviation between QSS simulations and DNS data at low Π_1 . This is primarily due to the influence of vortex shedding where this effect is not accounted in the QSS model.

3.2 Formulation of the non-dimensionalised parameters Π_1 and Π_2

The natural time scales of the system could be obtained by linearising the quasi-steady equation of motion. (Eq: ***KJ: equation of motion ***) and finding the eigenvalues. The non-linear terms of the forcing function are truncated and the equation of motion could be expressed as,

$$m\ddot{y} + c\dot{y} + ky = \frac{1}{2}\rho U^2 \mathcal{A}a_1 \left(\frac{\dot{y}}{U} \right), \quad (3.1)$$

After combining the \dot{y} terms and solving for eigenvalues the following solutions for the eigenvalues could be obtained.

$$\lambda_{1,2} = -\frac{1}{2} \frac{c - \frac{1}{2}\rho U \mathcal{A}a_1}{m} \pm \frac{1}{2} \sqrt{\left[\frac{c - \frac{1}{2}\rho U \mathcal{A}a_1}{m} \right]^2 - 4 \frac{k}{m}}. \quad (3.2)$$

Galloping essentially occurs at low frequencies therefore it can be assumed that the spring is relevantly weak and therefore, $k \rightarrow 0$. Hence a single non-zero eigenvalue remains which is,

$$\lambda = -\frac{c - \frac{1}{2}\rho U \mathcal{A}a_1}{m}. \quad (3.3)$$

Further, if it is assumed that the mechanical damping is weaker than the fluid dynamic forces on the body the non zero eigenvalue could be further simplified to,

$$\lambda = \frac{\frac{1}{2}\rho U \mathcal{A}a_1}{m}. \quad (3.4)$$

3. GOVERNING PARAMETERS OF FLUID-ELASTIC GALLOPING

In this representation λ represents the inverse time scale of the motion of the body due to the effect of long-time fluid dynamic forces (or forced due to the induced velocity). This term could also be re-written and λ could be expressed as

$$\lambda = \frac{a_1}{m^*} \frac{U}{D} \quad (3.5)$$

This form clearly shows the significant parameters that influences the inverse time scale of the system. $\partial C_Y / \partial \alpha$, the rate of change in the fluid dynamic force on the body, with respect to the induced angle of attack, is represented by a_1 . $\frac{U}{D}$ represents the inverse advective time scale of the incoming flow, and the mass ratio is resented by m^* . Increasing a_1 would result in a rapid change of the fluid dynamic force with a small change of the induced angle θ , which is proportional to transverse velocity \dot{y} . It can be seen in equation 3.5 that an increase of a_1 would result in an increase of the inverse time scale or decrease the response time of the body. In contrast the mass ratio has the opposite effect where an increase in m^* will lead to a decrease in λ , since a heavier body (or a body with higher inertia) would have a slower response.

In order to find the relevant dimensionless groups of the problem, the time scale formulated could be used to non-dimensionalise the equation of motion. The equation of motion presented in Equation ***KJ: put final equation of motion *** can be non-dimensionalised using the non dimensional time τ , defined as $\tau = t(a_1/m^*)(U/D)$. The non-dimensional equation of motion could then be represented as,

$$\ddot{Y} + \frac{m^{*2}}{a_1^2} \frac{kD^2}{mU^2} Y = \left(\frac{1}{2} - \frac{m^*}{a_1} \frac{cD}{mU} \right) \dot{Y} - \frac{a_1 A_3}{m^{*2}} \dot{Y}^3 + \frac{a_1^3 a_5}{m^{*4}} \dot{Y}^5 - \frac{a_1^5 a_7}{m^{*6}} \dot{Y}^7. \quad (3.6)$$

The equation could be further altered by regrouping the coefficients into non-dimentional groups and could be expressed as,

$$\ddot{Y} + \frac{4\pi^2 m^{*2}}{U^{*2} a_1^2} Y = \left(\frac{1}{2} - \frac{c^* m^*}{a_1} \right) \dot{Y} - \frac{a_1 A_3}{m^{*2}} \dot{Y}^3 + \frac{a_1^3 a_5}{m^{*4}} \dot{Y}^5 - \frac{a_1^5 a_7}{m^{*6}} \dot{Y}^7, \quad (3.7)$$

U^* is the reduced velocity which is the typical independent variable used in vortex-induced vibration studies. c^* is the non-dimensional damping parameter which is expressed as $c^* = cD/mU$.

By analysing equation 3.7 it is clear that five dimensionless parameters play a role in setting the response of the system. These are namely the stiffness, damping, mass ratio, the

geometry and the Reynolds number. The stiffness is represented by the reduced velocity U^* , the damping by c^* and the mass ratio by m^* . The geometry and the Reynolds number are represented by the coefficients a_n , of the polynomial fit to the C_y curve. Using the natural time scales of the system, grouping of these non-dimensional parameters into two groups in the non-dimensional equation of motion, suggests that there are two groups that govern the response which are: $\Gamma_1 = 4\pi^2 m^{*2}/U^{*2} a_1^2$ and $\Gamma_2 = c^* m^*/a_1$. Γ_1 could be described as a combined mass-stiffness, where Γ_2 could be expressed as a combined mass-damping parameter for a given geometry and a Reynolds number. It is assumed that the stiffness plays a minor role, Γ_2 seems more likely parameter to collapse the data. The wind tunnel data in the classic paper of galloping by (Parkinson and Smith, 1964) adopted a parameter similar to Γ_2 to collapse the data.

All of the quantities that formulate Γ_1 and Γ_2 except a_1 in theory, could be obtained before an experiment. However in order to obtain the value of a_1 static body experiments are required making it relatively difficult to obtain. Here, the Re and the geometry remains constant and therefore multiplying Γ_1 with a_1^2 and Γ_2 with a_1 suitable parameters could be obtained, and formulate a mass-stiffness parameter $\Pi_1 = 4\pi^2 m^{*2}/U^{*2}$, and a mass-damping parameter defined as $\Pi_2 = c^* m^*$. Therefore equation 3.7 can be written in terms of Π_1 and Π_2 .

$$\ddot{Y} + \Pi_1 Y = \Pi_2 \dot{Y} - \frac{a_1 a_3}{m^{*2}} \dot{Y}^3 + \frac{a_1^3 a_5}{m^{*4}} \dot{Y}^5 - \frac{a_1^5 a_7}{m^{*6}} \dot{Y}^7, \quad (3.8)$$

From equation 3.8, it is clear that the governing parameters of the non dimensionlised equation are Π_1 , Π_2 and m^* . However, from closer inspection it is possible to see that m^* has an impact on the non-linear terms of the forcing function. The velocity of the and hence the induced angle of attack needs to be very high in order for the non-linear terms to be applicable.

3.3 Quasi-steady state results

3.3.1 Classical VIV parameters vs. Π_1 and Π_2 .

Vortex-induced vibrations being another form fluid-structure interaction which occurs in a slender structure, has been investigated as candidate for power extraction from external

3. GOVERNING PARAMETERS OF FLUID-ELASTIC GALLOPING

flows. Significant progress on this problem have been made by Bernitsas et al. (2008, 2009); Raghavan and Bernitsas (2011); Lee and Bernitsas (2011) and other colleagues in VIVCACE group in the University of Michigan. Hence, it may seem that it is reasonable to present the data in a fluid-elastic problem using the same parameters in a VIV problem.

QSS data presented in figure 3.1 at $Re = 200$, shows a comparison between classical VIV and the newly formulated parameters presented as independent variables. The displacement amplitude, velocity amplitude and the mean power is presented in sub-figures (a), (c) and (e), as functions of the classical VIV parameter U^* for different ζ . The same data as functions of Π_2 , are presented in sub-figures (b), (d) and (f), for various, reasonably high values of Π_1 ***KJ: put the parameters used section***. Sub-figure (e) shows a similar trend to Barrero-Gil et al. (2010). The Value of the peak power remains constant. However, the power curve shifts to the right as ζ is increased. Here, in figure 3.1 the maximum dimensionless power is achieved at two times the velocity at which the galloping starts, which is similar to the observations made by Barrero-Gil et al. (2010); Vicente-Ludlam et al. (2014). An excellent collapse for velocity amplitude and mean power could be observed on the data, presented using the dimensionless group Π_2 , formulated using the natural time scales of the system. This implies that essentially velocity amplitude and the mean power is dictated by Π_2 which furthermore, implies that the natural frequency of the system which is used to scale U^* , ζ and Π_1 does not have a significant influence on the behaviour of the system, unlike VIV, which is a resonant phenomenon.

3.3.2 High and low Re data

The successful collapse of data, mean power in particular using Π_2 for low Reynolds number ($Re = 200$), could be replicated at high Reynolds numbers. An example case is presented in figure 3.1 at $Re = 22300$ for selected vales of Π_1 . The successful collapse of mean power data at high Reynolds numbers shows that suitability of using Π_2 as an independent variable across a large range of Reynolds numbers.

Hysteresis is evident in the high Reynolds number case ($Re = 22300$). Manipulating the initial condition (initial displacement) lead to obtaining different solutions for the same Π_2 value. The upper and lower branch were obtained by giving an initial displacement which was higher than the expected amplitude and providing a lower initial displacement

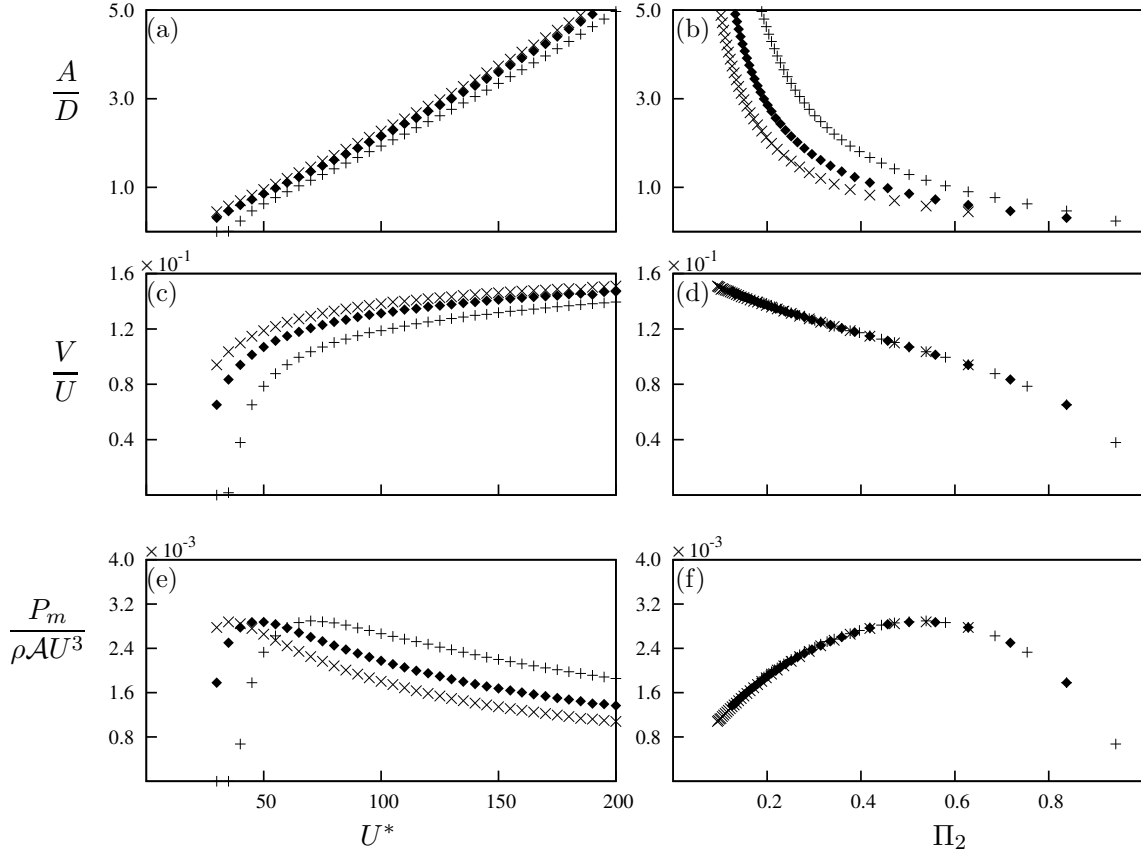


Figure 3.1: Displacement amplitude, velocity amplitude and dimensionless mean power data as functions of two different independent variables. Data presented in (a), (c) and (e) using the classical VIV parameter U^* , obtained at $Re = 200$ and $m^* = 20$ at three different damping ratios: $\zeta = 0.075$ (\times), $\zeta = 0.1$ (\blacklozenge) and $\zeta = 0.15$ ($+$). (b) (d) and (f) are the same data presented using the combined mass-damping parameter (Π_2) as the independent variable. Even though Π_1 varies in the range of $0.4 \leq \Pi_1 \leq 17.5$, it is clear that the power is a function of Π_2 only.

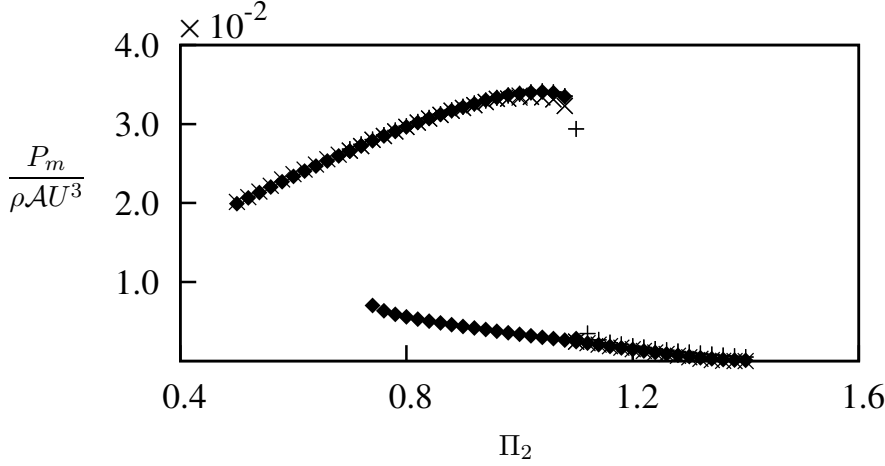


Figure 3.2: Dimensionless mean power as a function of Π_2 . Data presented at (a) $Re = 22300$, $\Pi_1 = 200$ (\times), $\Pi_1 = 2000$ (\blacklozenge) and $\Pi_1 = 10000$ ($+$). Hysteresis could be observed at high Re .

respectively. Even though in theory, there is a possibility of a third state, this unstable branch could not be achieved with a time integration method (also observed by (Vio et al., 2007)) such as the one employed in this study.

3.3.3 Dependence on mass-stiffness, Π_1

From the results of sections 3.3.1 and 3.3.2 shows essentially a single variable governs the mean extracted power, which is the combined mass-damping parameter, Π_2 . The time scale analysis carried out in section 3.2 shows that not only Π_2 but also Π_1 influences the system. Previous studies such as Bouclin (1977) have also reported a complex interaction between the displacement amplitude and the natural frequency, for high natural frequencies in particular; or in this instance equivalent to low values of Π_1 . This section investigates the impact of Π_1 further. The overall behavior of the system is divided into two regimes, one for “high” Π_1 and the other for “low” Π_1 and analysed.

The mean power as a function of Π_2 for a range of values of Π_1 is presented in figure 3.3. In the two subfigures presented, (a) shows the data for $\Pi_1 \geq 10$, while (b) shows data for $\Pi_1 \leq 10$. The excellent collapse in figure 3.3(a) shows that for $\Pi_1 \geq 10$, the mean power is independent of Π_1 .

In contrast figure 3.3(b) shows that for low values of $\Pi_1 \leq 10$, the predicted mean power

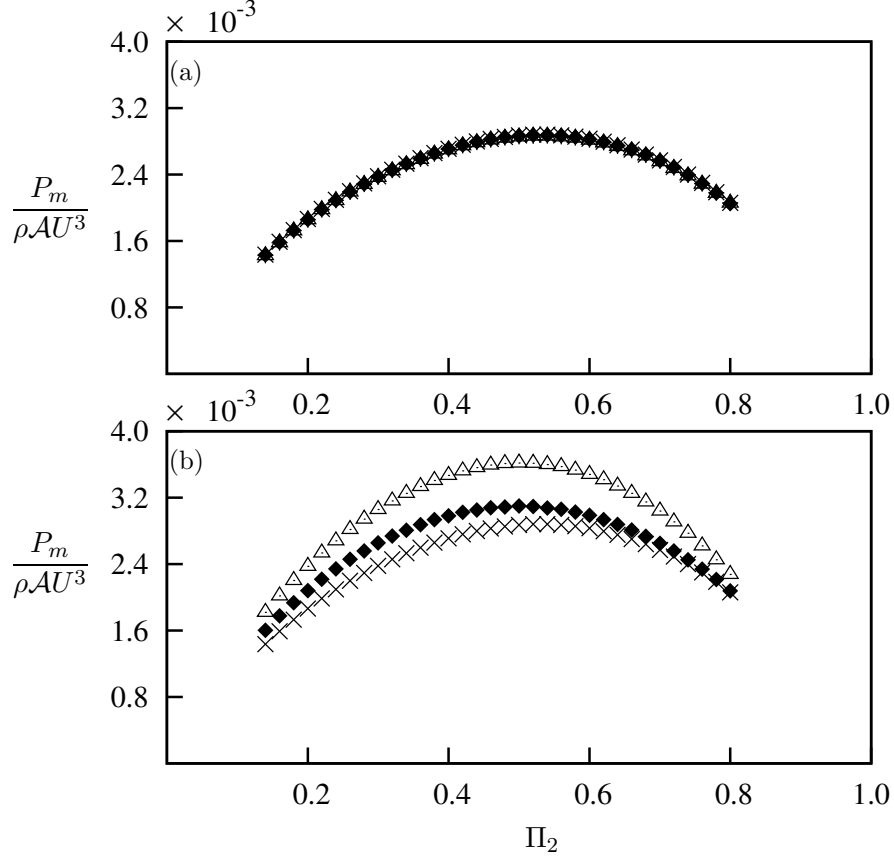


Figure 3.3: Dimensionless mean power as a function of Π_2 obtained using the QSS model at $Re = 200$. (a) High Π_1 ; data presented at four different combined mass-stiffness levels. $\Pi_1 = 10$ ($m^* = 20$, $U^* = 40$) (\times), $\Pi_1 = 100$ ($m^* = 80$, $U^* = 50$) ($+$), $\Pi_1 = 500$ ($m^* = 220$, $U^* = 60$) (\blacklozenge) and $\Pi_1 = 1000$ ($m^* = 400$, $U^* = 40$) (\triangle). (b) Low Π_1 ; data presented at $\Pi_1 = 10$ (\times), $\Pi_1 = 0.1$ (\blacklozenge), and $\Pi_1 = 0.01$ (\triangle).

3. GOVERNING PARAMETERS OF FLUID-ELASTIC GALLOPING

increases as Π_2 decreases. This indicates that at this region ($\Pi_1 < 10$), the mean power is a weak function of Π_1 ; hence, providing a distinction between high and low regimes of Π_1 . The mean extracted power is only a function of Π_2 where $\Pi_1 \geq 10$ or for high Π_1 . For low values, $\Pi_1 < 10$, the mean power becomes a strong function of Π_2 and a weak function of Π_1 .

It is clear that regardless of the value of Π_1 , the variation of power with Π_2 is essentially the same. As Π_2 is increased, the mean extracted power will increase to the point which, it will attain some maximum value and then decrease. This relationship between power and Π_2 could be explained by analysing the time histories of selected cases. AS an example, data at $\Pi_1 = 10$, $m^* = 20$ and $Re = 200$ are presented in figure 3.4. Three major regions where the value of the power curve are considered. These regions are Π_2 less than (region 1), equal to (region 2) and greater than (region 3) to the Π_2 value where the mean power is at its maximum.

The damping is low in region 1 ($\Pi_2 = 0.15$) in comparison with region 2 and 3. Although this may lead to larger oscillations, according to equation 2.1 damping is required to dissipate and therefore extract power. Hence, a low mean power output is gained at low damping. The high velocity amplitude leads the equivalent incident angle θ to exceed the positive range of C_y (i.e. $0 < \theta < 6^\circ$ as shown in figure 1.3(a)) resulting a negative dissipated power by damping P_d over some portion of the cycle as shown in figure 3.4 (a). The galloping force F_y and the transverse velocity \dot{y} are not in phase in this portion of the cycle where the force opposes the direction of travel. As a consequence, during this period of time the opposite of what is expected happens, where the power is transferred from the structure to the fluid. Since Π_2 is substantially low, from an energy perspective, the mechanical damping is not sufficient to remove the energy transferred from the fluid to the structure through work during other times of the cycle. Hence, as depicted by the negative region of P_d , this excess energy is transferred back to the fluid.

A clear sinusoidal signal of both P_d and P_t (3.4(c)) could be observed at region 3 where $\Pi_2 = 0.8$ and the damping constant is high. The equivalent incident angle θ (which for small values, is proportional to the transverse velocity of the body) is in phase with the galloping force F_y as shown in figures 3.4(f) and 3.4(i). The velocity amplitude is small in this case resulting θ falling within the range where the fluid-dynamic force (F_y) increases

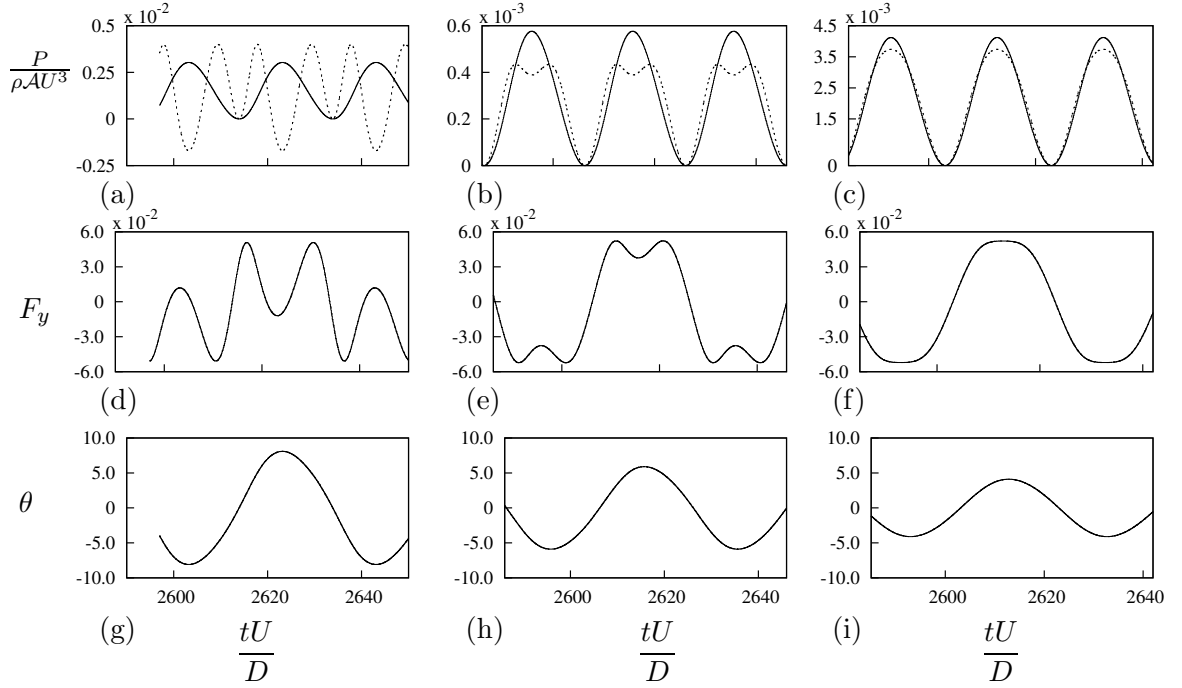


Figure 3.4: Time histories of P_t , P_d , F_y and θ at $\Pi_2 = 0.15, 0.54$ and 0.8 from the QSS model. Data was obtained at $m^* = 20$, $\Pi_1 = 10$ and $Re=200$. The time histories of P_t (—) and P_d (---) are presented for: (a) $\Pi_2 = 0.15$; (b) $\Pi_2 = 0.54$; (c) $\Pi_2 = 0.8$. Time histories of the instantaneous force F_y for: (d) $\Pi_2 = 0.15$; (e) $\Pi_2 = 0.54$; (f) $\Pi_2 = 0.8$. Time histories of the instantaneous angle θ for: (g) $\Pi_2 = 0.15$; (h) $\Pi_2 = 0.54$; (i) $\Pi_2 = 0.8$.

3. GOVERNING PARAMETERS OF FLUID-ELASTIC GALLOPING

within the incident angle (i.e. $0 < \theta \leq 5^\circ$ as shown in figure ??(a)). These conditions are favourable for high power output according to equation ?. Be that as it may, in this case the velocity is limited because of the high damping resulting relatively low fluid dynamic forcing.

A harmony between the high and low values of damping could be found at region 2 ($\Pi_2 = 0.54$). It is evident that P_d remains periodic but is not a pure sinusoidal signal. Two ‘peaks’ are present in a single half cycle from the time history graph of P_d as shown in figure 3.4(b). The velocity amplitude actually exceeds the equivalent incident angle where the fluid-dynamic forces peaks (i.e. $\theta = 5^\circ$ in 1.3 (a)) in this scenario. The dip in between the two peaks in a single half cycle correspond approximately to the time where the transverse velocity is higher than 0.09 and F_y is decreasing with increasing transverse velocity. As this region is the best compromise between region 1 and region 3, the maximum mean power could be attained in this region. Region 2 could also be identified as the “sweet spot” for energy extraction as the damping is high enough to obtain a high power output while not so high for the motion to be completely suppressed.

3.3.4 Dependence on the mass ratio m^*

It is clear that the mean extracted power is only a function of Π_2 for high values of Π_1 . However, the question remains about the region of low Π_1 . Does the variation of the mean extracted power occur purely as a function of Π_1 , or does the mass ratio also have an influence on power? The QSS model was solved by varying the values for m^* but keeping the Π_1 fixed. In other words Π_1 was changed by changing the stiffness of the system.

It is clear from figure 3.5, data presented being the mean extracted power as a function of Π_2 , for a fixed $\Pi_1 = 0.1$, for three different values of m^* , that mean power is independent of m^* , hence, it is only a function of Π_1 and Π_2 .

3.3.5 Comparison with DNS data

The QSS model assumes that the only force driving the system is the instantaneous lift generated by the induced velocity. However, vortex shedding is also present in this system. Therefore, an essential assumption when this model is used, is that the effect of vortex shedding is minimal. Hence, the model has been always used at high Re and at high mass

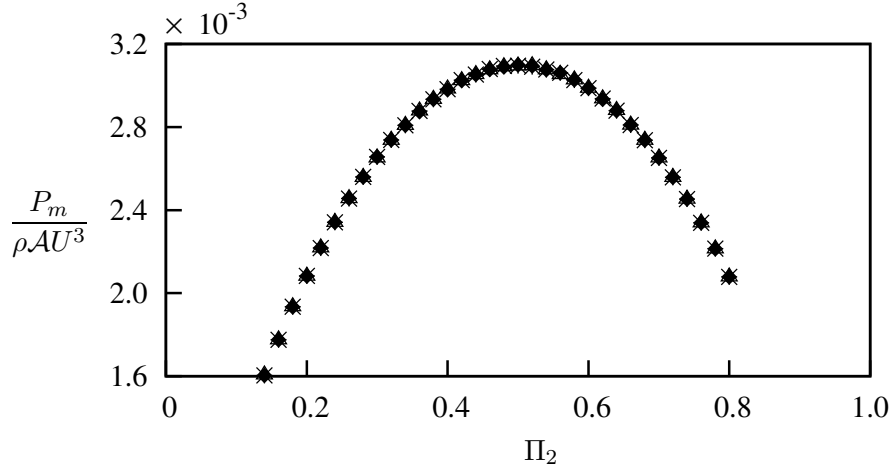


Figure 3.5: Dimensionless mean power as a function of Π_2 obtained using QSS model at $\Pi_1 = 0.1$. Data presented at $m^* = 2$ (\blacklozenge), $m^* = 20$ (\triangle) and $m^* = 50$ (*). The mass ratio does not have an effect on Π_1 even at low Π_1 .

ratios. The present study is focused on identifying the limiting parameters of the QSS model at low Reynolds numbers by providing a comparison with DNS results.

Joly et al. (2012) showed that the displacement data obtained using the QSS assumption and DNS agree well at low Reynolds numbers, with the modification implemented to the oscillator equation which accounts for the vortex shedding. These data were obtained at zero damping levels. However, the current study is focused on the behaviour and the power transfer of the system. Therefore analysing the behaviour of the system with increasing damping is of interest.

The comparison between QSS and the DNS results is presented in figure 3.6. The maximum displacement, velocity and mean extracted power are presented as a function of Π_2 . A range of values of Π_1 are compared to the QSS model data for $\Pi_1 = 10$. Figures 3.6(a) and 3.6(b) show little variation with Π_1 , and the comparison between the QSS model and the DNS simulations is quite good. However, the mean extracted power shown in figure 3.6(c) reveals that the mean power is influenced by both Π_1 and Π_2 . This is particularly clear for low values of Π_1 , where the discrepancy between the QSS model predictions of power and the DNS simulations is the largest. Comparing figure 3.6(c) with figure 3.3(a) shows that Π_1 has much more influence on the power extracted than predicted by the QSS model for low Π_1 values. In fact, the QSS model predicts that the mean extracted

3. GOVERNING PARAMETERS OF FLUID-ELASTIC GALLOPING

power should increase with decreasing Π_1 when Π_1 moves to the low Π_1 region (figure 3.3(b)), whereas the DNS simulations show that the mean extracted power decreases with decreasing Π_1 .

Figure 3.7(a) clearly shows the dependence of the mean extracted power on Π_1 . Here, the maximum power extracted for a given value of Π_1 , over all values of Π_2 (essentially the value of extracted power at the turning point), is plotted as a function of Π_1 . These values were obtained by fitting a quadratic to the data of figure 3.5 and finding the value of mean extracted power at the turning point. The rapid decrease in the extracted power as $\Pi_1 \rightarrow 0$ is clear.

Figure 3.7(a) also shows that Π_1 is important to higher values than predicted by the QSS model. For the QSS model, the mean extracted power was essentially independent of Π_1 for $\Pi_1 > 10$, as shown by the open symbols on the figure. However, the mean extracted power from the DNS data shows a significant dependence on Π_1 for $\Pi_1 < 250$. Even so, the power extracted during the DNS simulations converges to the value predicted by the QSS model as Π_1 increases.

Figure 3.7(b) shows the value of Π_2 at which the turning point, and therefore the maximum power output, occurs. The open symbols show the value predicted by the QSS model, the closed symbols show the value predicted by the DNS. The two are not the same, with a value around 0.41 predicted by the DNS (shown with a dashed line) and a value above 0.5 predicted by the QSS model. However, both models show that while the power extracted is a reasonably strong function of Π_1 , the value of Π_2 at which this maximum power occurs is relatively unaffected.

In an effort to further quantify the performance of the QSS model, the percentage between the QSS and DNS extracted power data as a function of Π_1 was calculated using the equation

$$\% \text{ error} = \left| \frac{P_{m(QSS)} - P_{m(DNS)}}{P_{m(DNS)}} \right| \times 100. \quad (3.9)$$

The results of this calculation are plotted in figure 3.8, along with a power-law best fit $138.697\Pi_1^{-0.6}$. The figure clearly shows that as Π_1 increases, the error between the QSS and DNS models quickly decreases. However, at low values of Π_1 , the discrepancy between the two can be quite large, around 30%.

A likely reason for this discrepancy at low Π_1 is the influence of the vortex shedding,

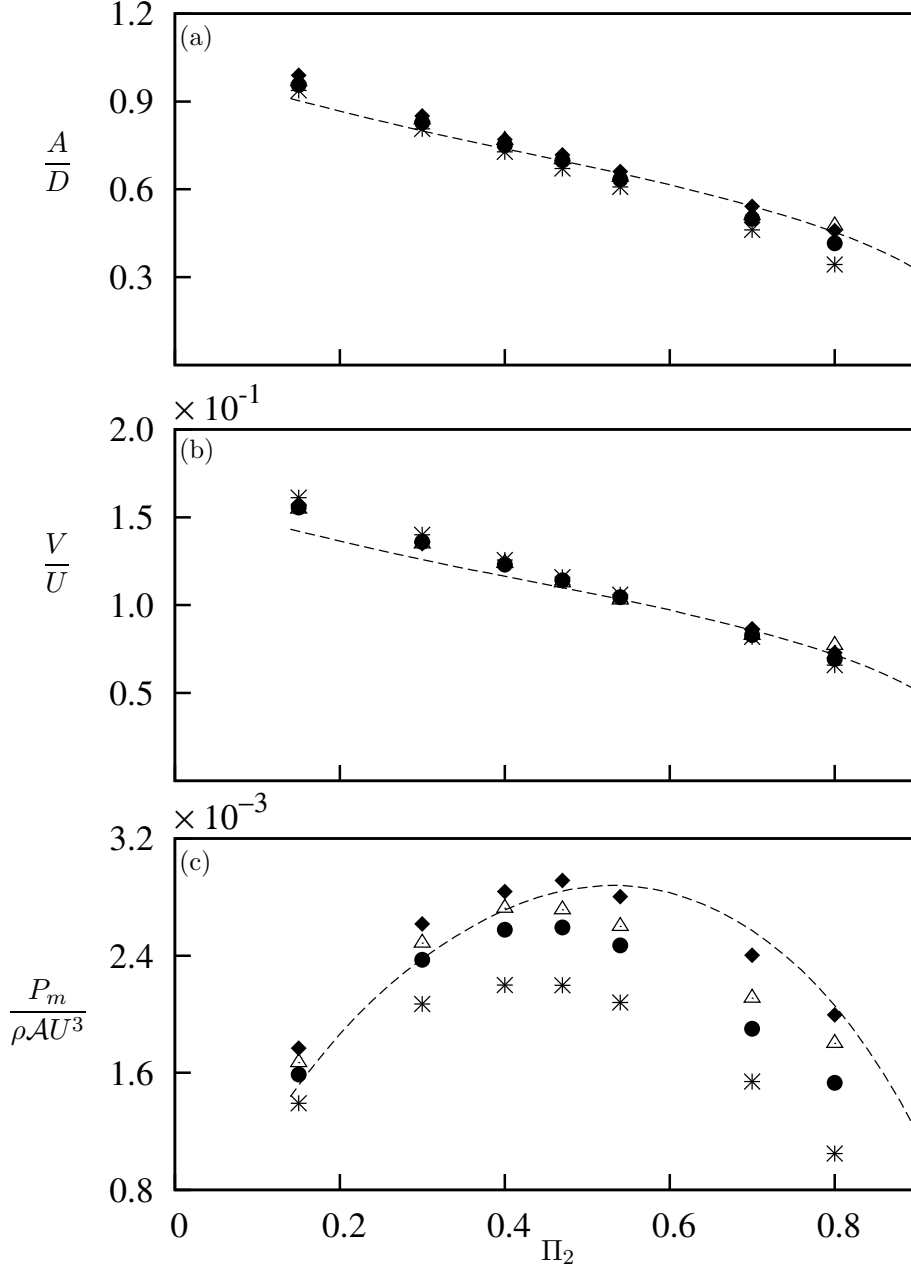


Figure 3.6: Comparison of data generated using the quasi-static model and full DNS simulations at (a) Displacement amplitude, (b) velocity amplitude and (c) dimensionless mean power as functions of Π_2 . Data were obtained at $Re = 200$ at four values $\Pi_1 = 10$ ($m^* = 20.13$) (*), $\Pi_1 = 60$ ($m^* = 49.31$) (●), $\Pi_1 = 250$ ($m^* = 100.7$) (△) and $\Pi_1 = 1000$ ($m^* = 201.3$) (◆). The QSS data at $\Pi_1 = 10$ (---).

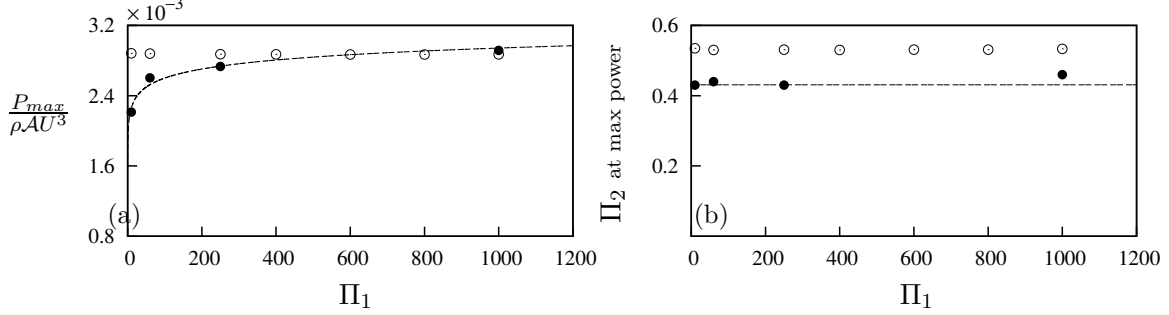


Figure 3.7: (a) Maximum power and (b) the value of Π_2 at maximum power of QSS data (○) and DNS data (●), as functions of Π_1 . For the DNS data, The maximum power asymptotes to an upper value with increasing Π_1 , while the value of Π_2 where maximum power occurs is relatively insensitive to Π_1 . The maximum power of the QSS data remains relatively constant, as does the value of Π_2 where maximum power occurs. The dash curve (---) of (a) follows the logarithmic fit of the maximum power which is $P_{max}/\rho AU^3 = 1.48 \times 10^{-4} \ln(\Pi_1) + 1.9 \times 10^{-3}$. The dashed curve in (b) shows the value $\Pi_2 \simeq 0.43$.

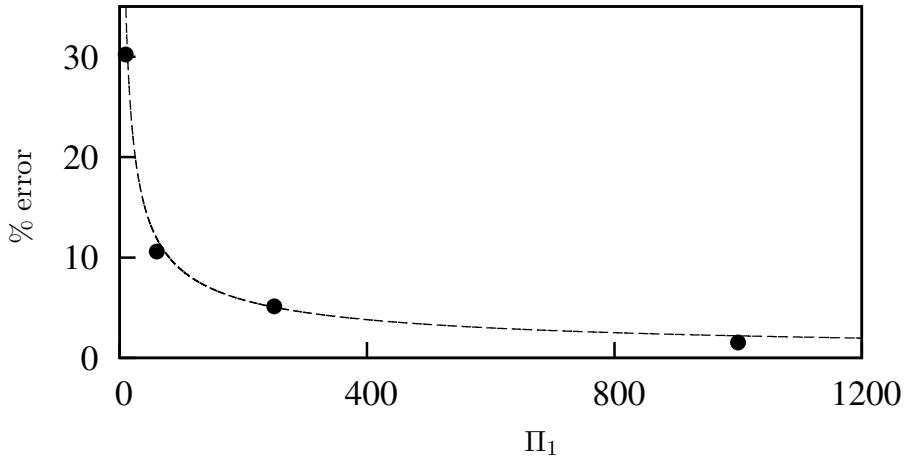


Figure 3.8: The percentage error between the maximum power obtained using DNS data and predicted by QSS model as a function of Π_1 . The QSS model prediction is worst for low values of Π_1 . The dash curve (---) follows the power law fit of the percentage error which is $\%error = 138.697\Pi_1^{-0.6}$.

which is not accounted for in the QSS model. To investigate this further, frequency spectra for the body velocity from DNS cases at varying values of Π_1 , at a value of $\Pi_2 = 0.47$ (close to the value at which the mean extracted power is a maximum), have been produced. They are presented, along with the original time histories in figure 3.9.

This figure shows the velocity signals at $\Pi_1 = 0.8$ and $\Pi_2 = 10, 60, 250$ and 1000 and the corresponding spectrum. The spectral data shows a significant component around $fd/U = 0.156$ which can be identified as the vortex shedding frequency. The magnitude of the component at the vortex shedding frequency clearly reduces as Π_1 is increased. This indicates that the influence of vortex shedding is much more prominent at low Π_1 , therefore resulting in larger deviations from quasi-steady state results. This builds on the work of Joly et al. (2012), which was conducted at zero damping, that implied that mean extracted power would be influenced by vortex shedding at low mass.

This influence is explicitly shown here. Figure 3.10 plots the relative intensity of the component at the vortex shedding frequency to the component at the galloping or oscillation frequency in the spectra of figure 3.9.

Similar to the discrepancy between the QSS and DNS mean extracted power shown in figure 3.8, the relative strength of the vortex shedding is seen to be large at small values of Π_1 , and quickly decreases as Π_1 is increased. The figure shows that the relative power of the vortex shedding frequency to the galloping frequency varies like $0.977\Pi_1^{-0.52}$.

The difference between the power predicted by the QSS and DNS models scales with $\Pi_1^{-0.6}$; the relative power at the vortex shedding frequency scales with $\Pi_1^{-0.52}$. These scalings are quite similar, and both are close to $1/\sqrt{\Pi_1}$. While not unequivocal, this correlation strongly indicates this discrepancy is due to the influence of the vortex shedding, even though the vortex shedding and galloping frequencies remain separated by around the same amount for all values of Π_1 presented in figure 3.9. The data presented in figure 3.10 also give some indication of the strength of any vortex shedding correction term that might be added to the QSS model in an effort to decrease the discrepancy between it and the DNS simulations.

Further information can be gained by observing the flow field. Flow field data at values of Π_2 close to where maximum power is produced at different Π_1 are presented in figure 3.11. The figure shows a clear wavelength of the wake as Π_1 is increased. Qualitatively, this

3. GOVERNING PARAMETERS OF FLUID-ELASTIC GALLOPING

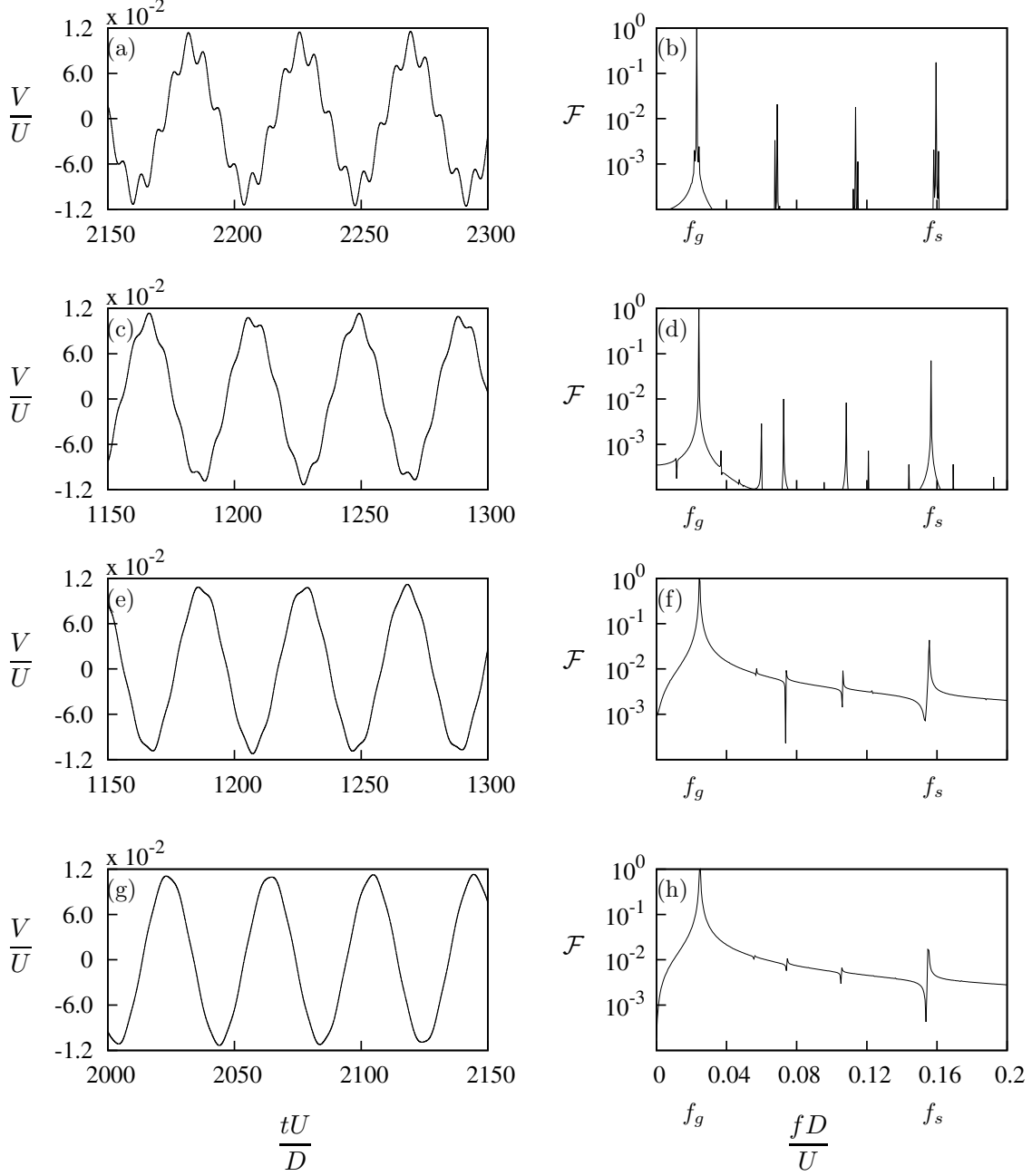


Figure 3.9: Velocity signal (right) and the corresponding power spectrum (left) of the DNS data at four values of Π_1 at $\Pi_2 = 0.47$. (a) and (b) $\Pi_1 = 10$, (c) and (d) $\Pi_1 = 60$, (e) and (f) $\Pi_1 = 250$, (g) and (h) $\Pi_1 = 1000$. U^* is kept at 40 therefore the mass ratio increases as Π_1 increases. It is evident that the influence of vortex shedding reduces as the inertia of the system increases.

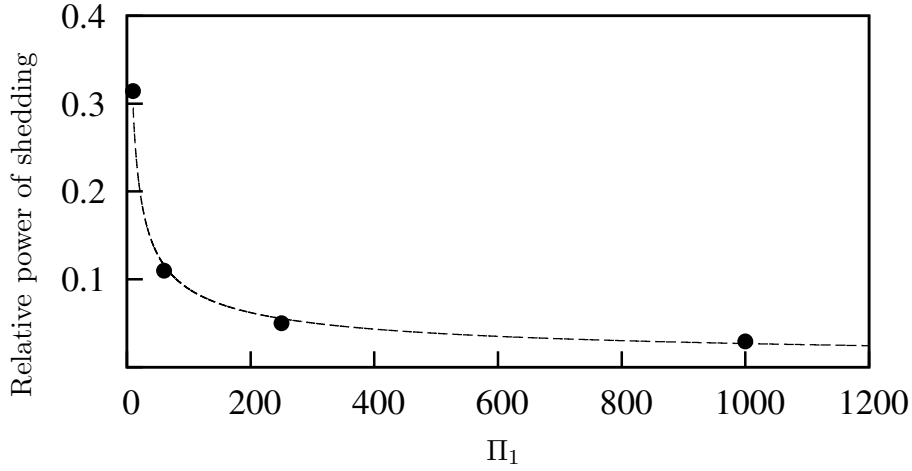


Figure 3.10: The relative power of the vortex shedding as a function of Π_1 . The relative power of the vortex shedding decreases as Π_1 increases. The dash curve (---) follows the power law fit of the percentage error which is $\text{Relative power} = 0.977\Pi_1^{-0.52}$.

can be interpreted as showing that at high Π_1 , the vortex shedding is simply superimposed over the path of motion of the cylinder. It shows a decrease in amplitude at low Π_1 , which may be due to the higher levels of non-linear interaction between the vortex shedding and galloping. Such an argument is consistent with the data of figure 3.10 that show the increasing significance of vortex shedding as Π_1 decreases. Taken together, this also goes some way to explaining the discrepancy between the output power predicted by the QSS and DNS models at low Π_1 , highlighted in figure 3.8.

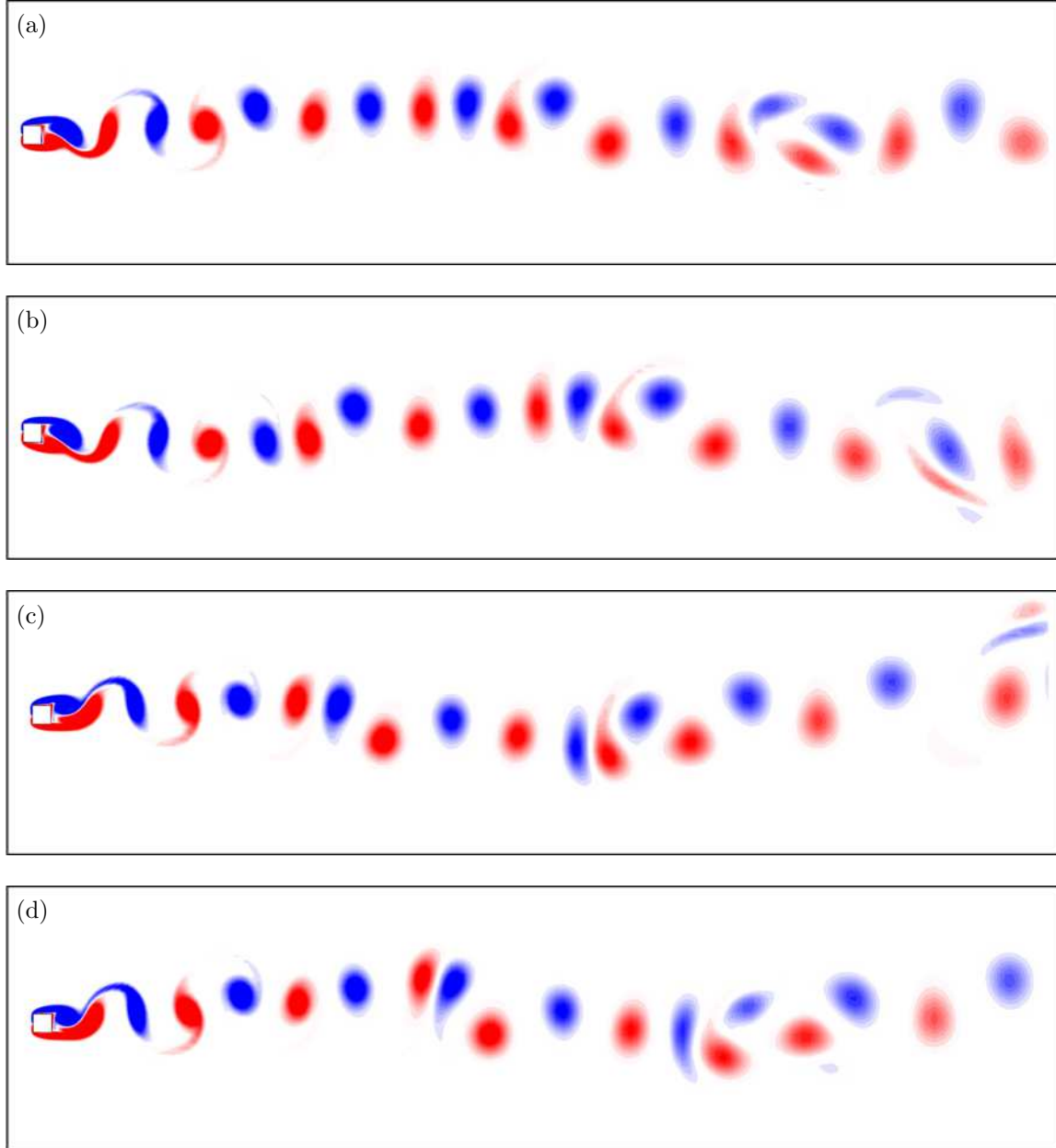


Figure 3.11: Vorticity plots of the flow at arbitrary instants at $\Pi_2 = 0.47$. (a) $\Pi_1 = 10$, (b) $\Pi_1 = 60$ (c) $\Pi_1 = 250$ and (d) $\Pi_1 = 1000$ at $Re = 200$. Contours show vorticity at levels between ± 1 .

BIBLIOGRAPHY

- Alonso, G., Meseguer, J., Pérez-Grande, I., 2005. Galloping instabilities of two-dimensional triangular cross-section bodies. *Experiments in Fluids* 38, 789–795.
- Alonso, G., Meseguer, J., Sanz-Andrés, A., Valero, E., 2010. On the galloping instability of two-dimensional bodies having elliptical cross-sections. *Journal of Wind Engineering and Industrial Aerodynamics* 38, 789–795.
- Alonso, G., Valero, E., Meseguer, J., 2009. An analysis on the dependence on cross section geometry of galloping stability of two-dimensional bodies having either biconvex or rhomboidal cross sections. *European Journal of Mechanics B/Fluids* 28, 328–334.
- Barrero-Gil, A., Alonso, G., Sanz-Andres, A., Jul. 2010. Energy harvesting from transverse galloping. *Journal of Sound and Vibration* 329 (14), 2873–2883.
- Barrero-Gil, A., Sanz-Andrés, A., Roura, M., Oct. 2009. Transverse galloping at low Reynolds numbers. *Journal of Fluids and Structures* 25 (7), 1236–1242.
- Bearman, P. W., Gartshore, I. S., Maull, D. J., Parkinson, G. V., 1987. Experiments on flow-induced vibration of a square-section cylinder. *Journal of Fluids and Structures* 1, 19–34.
- Bernitsas, M. M., Ben-Simon, Y., Raghavan, K., Garcia, E. M. H., 2009. The VIVACE Converter: Model Tests at High Damping and Reynolds Number Around 10^5 . *Journal of Offshore Mechanics and Arctic Engineering* 131 (1), 011102.
- Bernitsas, M. M., Raghavan, K., Ben-Simon, Y., Garcia, E. M. H., 2008. VIVACE (Vortex Induced Vibration Aquatic Clean Energy): A new concept in generation of clean and

BIBLIOGRAPHY

- renewable energy from fluid flow. *Journal of Offshore Mechanics and Arctic Engineering* 130 (4), 041101–15.
- Blevins, R. D., 1990. *Flow-Induced Vibration*, 2nd Edition. New York: Van Nostrand Reinhold.
- Bouclin, D. N., 1977. Hydroelastic oscillations of square cylinders. Master's thesis, University of British Columbia.
- Den Hartog, J. P., 1956. *Mechanical Vibrations*. Dover Books on Engineering. Dover Publications.
- Deniz, S. and Staubli, T., 1997. Oscillating rectangular and octagonal profiles: Interaction of leading-and trailing-edge vortex formation. *Journal of Fluids and Structures* 11, 3–31.
- Glauert, H., 1919. The rotation of an aerofoil about a fixed axis. Tech. rep., Advisory Committee on Aeronautics R and M 595. HMSO, London.
- Gresho, P. M., Sani, R. L., 1987. On pressure boundary conditions for the incompressible Navier–Stokes equations. *International journal for numerical methods in fluids* 7, 1111–1145.
- Griffith, M. D., Leontini, J. S., Thompson, M. C., Hourigan, K., 2011. Vortex shedding and three-dimensional behaviour of flow past a cylinder confined in a channel. *Journal of Fluids and Structures* 27 (5-6), 855–860.
- Joly, A., Etienne, S., Pelletier, D., Jan. 2012. Galloping of square cylinders in cross-flow at low Reynolds numbers. *Journal of Fluids and Structures* 28, 232–243.
- Karniadakis, G. E., Sherwin, S., 2005. *Spectral/hp element methods for computational fluid dynamics*, ii Edition. Oxford University.
- Kreyszig, E., 2010. *Advanced Engineering Mathematics*, 10th Edition. John Wiley & Sons.
- Lee, J., Bernitsas, M., Nov. 2011. High-damping, high-Reynolds VIV tests for energy harnessing using the VIVACE converter. *Ocean Engineering* 38 (16), 1697–1712.
- Lee, J., Xiros, N., Bernitsas, M., Apr. 2011. Virtual damperspring system for VIV experiments and hydrokinetic energy conversion. *Ocean Engineering* 38 (5-6), 732–747.

- Leontini, J. S., Lo Jacono, D., Thompson, M. C., Nov. 2011. A numerical study of an inline oscillating cylinder in a free stream. *Journal of Fluid Mechanics* 688, 551–568.
- Leontini, J. S., Thompson, M. C., 2013. Vortex-induced vibrations of a diamond cross-section: Sensitivity to corner sharpness. *Journal of Fluids and Structures* 39, 371–390.
- Leontini, J. S., Thompson, M. C., Hourigan, K., Apr. 2007. Three-dimensional transition in the wake of a transversely oscillating cylinder. *Journal of Fluid Mechanics* 577, 79.
- Luo, S., Chew, Y., Ng, Y., Aug. 2003. Hysteresis phenomenon in the galloping oscillation of a square cylinder. *Journal of Fluids and Structures* 18 (1), 103–118.
- Nakamura, Y., Mizota, T., 1975. Unsteady lifts and wakes of oscillating rectangular prisms. *ASCE Journal of the Engineering Mechanics Division* 101, 855–871.
- Nakamura, Y., Tomonari, Y., 1977. Galloping of rectangular prisms in a smooth and in a turbulent flow. *Journal of Sound and Vibration* 52, 233–241.
- Naudascher, E., Wang, Y., 1993. Flow induced vibrations of prismatic bodies and grids of prisms. *Journal of fluids and structures* 7, 341–373.
- Ng, Y., Luo, S., Chew, Y., Jan. 2005. On using high-order polynomial curve fits in the quasi-steady theory for square-cylinder galloping. *Journal of Fluids and Structures* 20 (1), 141–146.
- Païdoussis, M., Price, S., de Langre, E., 2010. *Fluid-Structure Interactions : Cross-Flow-Induced Instabilities*. Cambridge University Press.
- Parkinson, G., 1989. Phenomena and modelling of flow-induced vibrations of bluff bodies. *Progress in Aerospace Sciences* 26, 169–224.
- Parkinson, G., Brooks, N. P. H., 1961. On the aeroelastic instability of bluff cylinders. *Journal of Applied Mechanics* 28, 252–258.
- Parkinson, G. V., 1974. Mathematical models of flow-induced vibrations of bluff bodies. In *Flow-Induced Structural Vibrations*, e. naudascher Edition. Berlin: SpringerVerlag.
- Parkinson, G. V., Smith, J. D., 1964. The square prism as an aeroelastic non-linear oscillator. *The Quarterly Journal of Mechanics and Applied Mathematics* 17 (2), 225–239.

BIBLIOGRAPHY

- Raghavan, K., Bernitsas, M., Apr. 2011. Experimental investigation of Reynolds number effect on vortex induced vibration of rigid circular cylinder on elastic supports. *Ocean Engineering* 38 (5-6), 719–731.
- Raghavan, K., Bernitsas, M. M., Maroulis, D. E., 2009. Effect of Bottom Boundary on VIV for Energy Harnessing at $8 \times 10^3 < Re < 1.5 \times 10^5$. *Journal of Offshore Mechanics and Arctic Engineering* 131 (3), 031102.
- Robertson, I., Li, L., Sherwin, S. J., Bearman, P. W., 2003. A numerical study of rotational and transverse galloping rectangular bodies. *Journal of Fluids and Structures* 17, 681 – 699.
- Ruscheweyh, H., Hortmanns, M., Schnakenberg, C., 1996. Vortex-excited vibrations and galloping of slender elements. *Journal of Wind Engineering and Industrial Aerodynamics* 65, 347–352.
- Sheard, G. J., Fitzgerald, M. J., Ryan, K., Jun. 2009. Cylinders with square cross-section: wake instabilities with incidence angle variation. *Journal of Fluid Mechanics* 630, 43.
- Thompson, M., Hourigan, K., Sheridan, J., Feb. 1996. Three-dimensional instabilities in the wake of a circular cylinder. *Experimental Thermal and Fluid Science* 12 (2), 190–196.
- Thompson, M. C., Hourigan, K., Cheung, A., Leweke, T., Nov. 2006. Hydrodynamics of a particle impact on a wall. *Applied Mathematical Modelling* 30 (11), 1356–1369.
- Tong, X., Luo, S., Khoo, B., Oct. 2008. Transition phenomena in the wake of an inclined square cylinder. *Journal of Fluids and Structures* 24 (7), 994–1005.
- Tu, J., Yeoh, G., Liu, C., 2008. *Computational Fluid Dynamics: A Practical Approach*, 1st Edition. Butterworth-Heinemann.
- Vicente-Ludlam, D., Barrero-Gil, A., Velazquez, A., 2014. Optimal electromagnetic energy extraction from transverse galloping. *Journal of Fluids and Structures* 51, 281–291.
- Vio, G., Dimitriadis, G., Cooper, J., Oct. 2007. Bifurcation analysis and limit cycle oscillation amplitude prediction methods applied to the aeroelastic galloping problem. *Journal of Fluids and Structures* 23 (7), 983–1011.

- Weaver, D. S., Veljkovic, I., 2005. Vortex shedding and galloping of open semi-circular and parabolic cylinders in cross-flow. *Journal of Fluids and Structures* 21, 65–74.